



Design and testing of a new microinjector with FBG force sensor for robot-assisted single cell microinjection

Xiangyu Guo^{a,d}, Antian Zhao^a, Youchao Zhang^{a,d}, Huanyu Jiang^{a,d}, Limin Zeng^c, Alois Knoll^b, Yibin Ying^{a,d}, Mingchuan Zhou^{a,b,d,*}

^a Robotic Micro-nano Manipulation Lab, College of Biosystems Engineering and Food Science, Zhejiang University, Hangzhou, China

^b School of Computation, Information and Technology, Technische Universität München, München, Germany

^c The School of Software Technology, Zhejiang University, Hangzhou, China

^d Key Laboratory of Intelligent Equipment and Robotics for Agriculture of Zhejiang Province, Hangzhou, China

ARTICLE INFO

Keywords:

Microinjection
Force sensing
Cell manipulation
Robot-assisted
Fiber Bragg grating

ABSTRACT

Microinjection with force sensing has demonstrated robust performance in improving the cell survival rate and adjusting robot motion parameters. In this article, a novel force-sensing microinjector is presented based on fiber Bragg grating (FBG) sensors to precept three-dimensional (3D) forces. Fibers are processed with acid to become thinner and more sensitive. Three optical fibers are affixed to the outer surface of the glass needle along the axial direction. Benefiting from the novel configuration of the FBG sensors, the hollow channel of the glass needle can be used to inject exogenous substances. Moreover, a prototype has been fabricated for the experiment. Experimental results demonstrate the proposed force sensor can achieve a resolution of 66.8 μN for puncture forces. Repeatability and temperature compensation experiments show the force sensor can provide a consistent and accurate measurement. The developed force sensor has been applied to the microinjection of the zebrafish embryos, which is a promising tool for perceiving cell manipulation microforces.

1. Introduction

Robot-assisted cell microinjection has wide applications in biological breeding, assisted reproduction, and cell analysis [1–3]. It provides high efficiency and high consistency compared with manual cell injection. At present, the robot-assisted cell microinjection has two main approaches, namely microinjection with pure vision and microinjection with force feedback [4–6]. However, the pure vision approach is based on cell deformation features, which cannot be used to reliably judge whether the cells are successfully punctured or not. While the force feedback approach has been demonstrated to have superior recognition of cell puncture status and significantly improve cell survival rate [7–9]. Moreover, the motion parameters and puncture force of the robot can be adjusted based on the force feedback [10–13].

Researchers have developed various microforce sensors, which are classified as contact sensors and non-contact sensors, e.g., visual force, capacitive force sensor, piezoelectric force sensor, and piezoresistive force sensor [10,11,14,15]. The visual force sensor is a type of non-contact sensor based on the mechanical model and image information. However, the mechanical behavior of the cell is complicated, e.g., elastic, nonlinear, and time-varying, which is a very challenging task

to establish a reliable cell model [16–18]. The optical sensor is another non-contact sensor, including force measurement based on the cantilever approach and force measurement based on the laser trap approach [19–21]. It can achieve ultrahigh sensing resolution ($p\text{N} - n\text{N}$). However, the main limitation is that this sensor has a small measure range and requires adequate cantilever reflectivity.

Concerning contact sensors, capacitive sensors convert the force applied in the probe into detectable capacitance, which is transformed into voltage changes with an electronic circuit. This sensor is up to sub-micronewton or sub-nanonewton level [22–24]. However, this sensor probe is too fragile to be easily damaged, and it is difficult to integrate with the glass needle to meet the requirements of cell injection. To monitor the puncture force during cell injection, Nan et al. [8] proposed a piezoelectric force sensor for automated multi-cell injection, the resolution of the calibrated force sensor is about 0.2 mN. It has an obvious step change in the force signal, which determines whether the cell is pierced. The piezoelectric plate has high stiffness and requires a higher resonant frequency, and the force sensing method based on the cantilever beam structure will cause secondary damage to cells. Wei et al. [25] presented a piezoresistive force-sensing microinjector with a compliant mechanism. The capacity of lateral loading (at least

* Corresponding author at: Robotic Micro-nano Manipulation Lab, College of Biosystems Engineering and Food Science, Zhejiang University, Hangzhou, China.
E-mail address: mczhou@zju.edu.cn (M. Zhou).

Table 1
Design specifications of the proposed sensor.

Index	Requirements
Performance	Resolution < 200 μN ; range > 0.6 mN
Size	Diameter = 1 ± 0.1 mm; Optical grating length < 15 mm
Sampling rate	> 100 Hz
Additional requirements	A hollow channel for injection

1 N) is achieved by the small-stiffness mechanism design with multiple compliant mechanisms (resolution: 1.2 mN). These sensors are difficult to be directly installed on the micromanipulator, which requires to design of special fixtures. In addition, the previous work mainly relied on the physical amplifying element and the flexible microstructure deformation to measure the single-dimensional force, but it lacks the capacity of three-dimensional (3D) microforce perception.

To this end, a novel force-sensing microinjection based on FBG sensors. The off-the-shelf fibers are processed to become thinner and more sensitive. Three optical fibers are affixed to the outer surface of the glass needle along the axial direction. Benefiting from the novel configuration of the FBG sensors, the hollow channel of the glass needle can be used to inject exogenous substances. The feature and contributions of the work are listed as follows:

- (1) The proposed sensor can detect 3D forces with an ingenious structure during microinjection. Not only can it be highly integrated with the injection needle, but it can inject exogenous substances into the cell through a central channel.
- (2) The prototype has been fabricated for experimental testing. Experimental results demonstrate the proposed force sensor can achieve a resolution of 66.8 μN for puncture forces. Repeatability and temperature compensation experiments show the force sensor can provide a consistent and accurate measurement.
- (3) Based on the developed sensor, a cell deformation model is developed, which explores the relationship between cell deformation, puncture velocity, and puncture force. It can be applied to cell low-damage manipulation research in the future.

In the following parts of the paper, Section 2 introduces the materials and methods of the designed sensor. In Section 3, the experiment and results of the force sensor have been carried out for injecting zebrafish embryos. Section 4 discusses this work. Section 5 concludes this article.

2. Materials and methods

The section illustrates the development of a force sensor in detail. First, the design requirement and structure of the prototype sensor are described. Second, the mechanical estimation model is established to calculate the puncture force. Third, the experimental setup is designed and fabricated for the proposed force sensor.

2.1. Design requirements

In this work, a new microforce sensor is proposed to detect microforce during cell injection. For illustration, zebrafish embryo cells are selected as the research object which is a popular biological model in biomedical study [26]. For injection proposes, a hollow channel is necessary for delivering an exogenous substance into cells, which is the main design challenge. Table 1 summarized detailed design parameters of the microinjector.

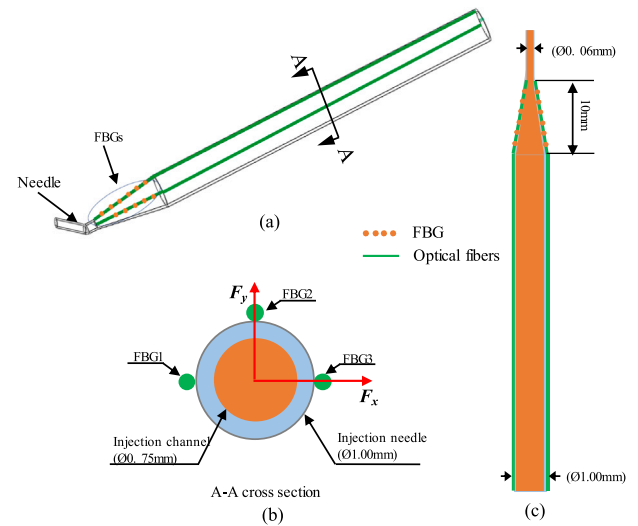


Fig. 1. Schematic structure of the prototype sensor. (a) CAD model of the needle with the 3-DOF force sensor. (b) Cross-section view. (c) Detailed design of this sensor.

The size of the zebrafish embryo cell is about 1 mm. According to the literature [27,28], the measurement range of the sensor is micronewton to sub-micronewton, and the resolution is above μN to meet the requirements. The thin glass needle is an elastomer and the force on the tip is more significant than other parts of the needle, the force sensor should be as close to the tip as possible.

2.2. Structure design of the prototype sensor

The detailed design of the proposed force sensor is described in Fig. 1. The glass needle diameter is 1 mm with a length of 5 cm. The angle between the tip and the vertical direction is 30° and the tip diameter is 60 to 80 μm . Three optical fibers with a diameter of 0.1 mm are distributed along the glass tube shaft to sense the wavelength shift by deflection of the glass tube. As depicted in Fig. 1, they are labeled as FBGs-1, FBGs-2, and FBGs-3. FBGs-2 is distributed on the central axis of the glass needle, which maintains a 90° angle between it and FBGs-1 and FBGs-3. Three optical fibers are attached to the surface of the glass needle with medical glue. The hollow channel of the glass needle can ensure the flow of liquid. The optical grating length of the FBG is 10 mm, the length of the glass needle is 50 mm, the diameter of the needle tip is 0.06 mm, and the diameter of the glass needle is 1 mm. The detailed information of the sensor is shown in the computer-aided design (CAD) model.

2.3. Mechanical estimation model

2.3.1. Transverse force calculation

The strain of the FBG sensor is linearly related to the torque and proportional to the transverse force applied to the needle tip [29]

$$\epsilon = \frac{M}{EI} \gamma = \frac{F_t d}{EI} \gamma \quad (1)$$

where ϵ is the local strain at the FBG sensor, and M denotes the bending torque attributed to the transverse force. F_t is the force applied to the needle tip, d is the distance between the needle tip and the FBG sensor, E is Young's modulus (about 70 GPa) [30], I represents the torque of inertia, and γ is the radial distance between the bending neutral axis and the FBG sensor.

The Bragg wavelength of the FBG sensor is linearly related to local strain and temperature change

$$\Delta\lambda = k_\epsilon \epsilon + k_{\Delta T} \Delta T \quad (2)$$

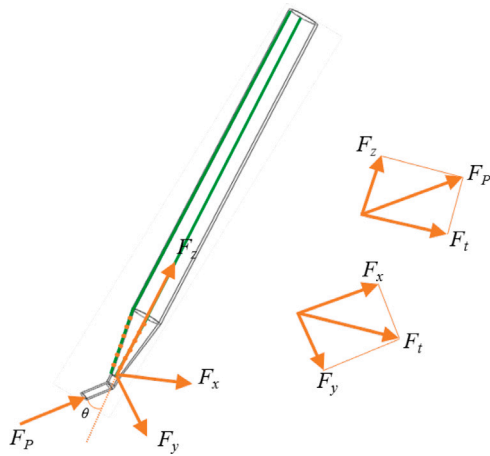


Fig. 2. Schematic diagram of mechanical analysis.

where $\Delta\lambda$ is the shift in Bragg wavelength, ΔT is the temperature change, k_ϵ and $k_{\Delta T}$ are constant-coefficient associated with strain and temperature, respectively.

Due to the FBG wavelength signal being cross-sensitive to temperature and strain, a temperature compensation algorithm is designed to reduce the sensitivity of FBG central wavelength to the environment temperature change. The relative wavelength change Δs_i is

$$\Delta s_i = \Delta\lambda_i - \Delta\lambda_{mean} = k_{\epsilon i} \epsilon_i - \frac{1}{3} \sum_{i=1}^3 k_{\epsilon i} \epsilon_i \quad (3)$$

where Δs_i is the relative wavelength change of the FBG sensor i , $\Delta\lambda_i$ is the shift wavelength of the FBG sensor i , $\Delta\lambda_{mean}$ is the average value of three FBG wavelength shifts, $k_{\epsilon i}$ is the strain coefficient, and ϵ_i is the local strain of FBG sensor i associated with transverse force, and i is 1, 2, and 3.

Combining Eqs. (1)–(3), the equation between the transverse force F_t and the shift wavelength of the FBG sensor is

$$F_t = K_t \Delta S_t \quad (4)$$

$$F_t = [F_x \ F_y]^T \quad (5)$$

$$\Delta S_t = [\Delta S_1 \ \Delta S_2 \ \Delta S_3]^T \quad (6)$$

where F_x and F_y are the transverse force, ΔS_t denotes the shift wavelength of the FBG sensor, K_t is a 2×3 coefficient matrix.

2.3.2. Axial force calculation

Given the mechanical relation in Fig. 2, axial force F_z is calculated as

$$F_z = \frac{F_t}{\tan \theta} \quad (7)$$

where F_z is the axial force, θ is the angle between F_p and F_z . The puncture force F_p is calculated as

$$F_p = \frac{F_t}{\sin \theta} \quad (8)$$

2.4. Experiment setup

As depicted in Fig. 3, the FBG micro force sensor calibration platform consists of an electronic balance (Haozhan, resolution: 0.0001 g, range: 0–200 g, Ruian Ante Weighing Equipment Co., LTD), a four channel of FBG sensor decoder (Tv-1600, sampling frequency: 1000 Hz, resolution: 1 pm, Beijing Tongwei Technology Co., LTD), a monitor, a 3-DOF robotic arm (TransferMan 4r, Eppendorf Inc., Germany), and

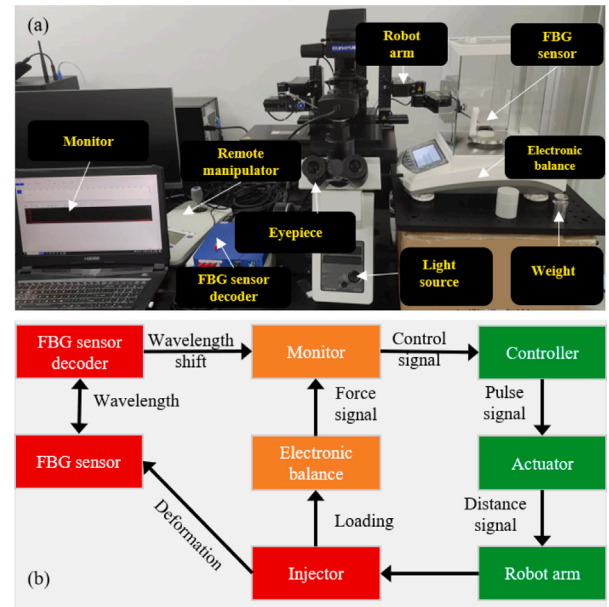


Fig. 3. Experiment setup of the FBG micro force sensor calibration platform. (a) FBG micro force sensor calibration platform. (b) System control diagram.

an FBG sensor (Wavelength range: 1510–1590 nm, signal noise ratio: > 15 dB, optical grating length: 10 mm, Beijing Tongwei Technology Co., LTD).

The controller sends a pulse signal to the driver, which controls the height of the robot arm. The injection needle is attached to the robot arm, and the FBG sensors contribute to shifting wavelength under the needle deformation. The wavelength shift is received and saved by the FBG sensor decoder. At the same time, the electronic balance record the gravity reading at this time. The FBG sensor generates wavelength shifts under needle deformation. The decoder reads and saves the wavelength shift, and the electronic scale records the gravity reading at this time.

The computer controls the robot arm to translate and rotate the sensor to adjust the magnitude and direction of the force load. A 1g weight is fixed on the tip of the needle. The tip loading weight is realized by changing the height of the mechanical arm. The rubber sheet prevents the glass needle from sliding under the load. During calibration, the pitch angle α ranging from $\pm(30^\circ-90^\circ)$ with 15° intervals, and the roll angle β ranging from $0^\circ-90^\circ$ with 15° intervals (Fig. 4). The force magnitude ranges from 0.2–1 g with 0.2 intervals. The calibration experiment is repeated three times. A total of 350 samples are collected from 70 force directions. These values obtained at each experiment are used to determine the calibration matrix K_t . There are many solutions regarding the calibration matrix K_t , however, not all coefficient matrices are optimal. In order to obtain the best estimate of the coefficient matrix K_t , the least square method is used to fit the coefficient matrix K_t .

2.5. Evaluation index

Residual e_i is the difference between observed value X_i and predicted value \hat{X}_i of the dependent variable. It is calculated as

$$e_i = X_i - \hat{X}_i \quad (9)$$

Coefficient of variation CV reflects the absolute value of data dispersion, which can be used to judge the stability of this proposed sensor. It can be expressed as

$$CV = \frac{SD}{\bar{X}} \quad (10)$$

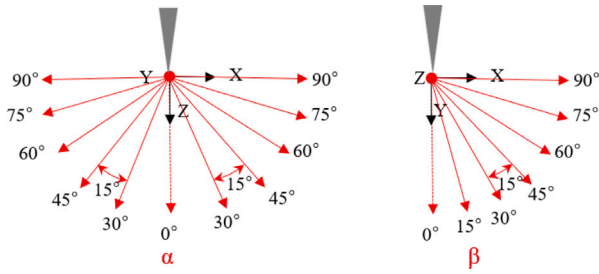


Fig. 4. Roll angle α and pitch angle β diagram. The pitch angle α ranging from $\pm(30^\circ-90^\circ)$ with 15° intervals, and the roll angle β ranging from $0^\circ-90^\circ$ with 15° intervals.

$$SD = \sqrt{\frac{1}{N-1} \sum_{i=1}^N (X_i - \bar{X})^2} \quad (11)$$

where SD is the standard deviation, N represents the total number of data samples. X_i represents the N th data. \bar{X} is the average of all data. The determination coefficient R^2 can evaluate the prediction ability of the model. It can be expressed as

$$R^2 = 1 - \frac{\sum_{i=1}^N (\hat{X}_i - X_i)^2}{\sum_{i=1}^N (\hat{X}_i - \bar{X}_i)^2} \quad (12)$$

The normal distribution function $f(x)$ evaluates the sensor data distribution, which can be written as

$$f(x) = \frac{1}{\sqrt{2\pi}\sigma} e^{-\frac{(x-\mu)^2}{2\sigma^2}} \quad (13)$$

Normal distribution function $P(X \leq x)$ for the interval $[-\infty, x]$ is

$$P(X \leq x) = \frac{1}{\sqrt{2\pi}\sigma} \int_{-\infty}^x e^{-\frac{(t-\mu)^2}{2\sigma^2}} dt \quad (14)$$

where σ is the scale parameter of normal distribution, which describes the dispersion degree of data distribution of normal distribution data. μ is the position parameter of the normal distribution, which describes the central tendency position of the normal distribution. t is the integral variable.

3. Experiments and results

3.1. Repeatability

To verify the consistency of the designed sensor response, 40 directional samples are randomly selected from all calibrated samples, including 15,865 data (total 3173 subsets). Each sample has the same force direction and magnitude. The mean and residual error of FBG wavelength shift is calculated. Then, the residual errors of all subsets are combined to calculate the standard deviation for each FBG sensor as a measure of repeatability.

As depicted in Fig. 5, we illustrate the probability distribution of wavelength shift residuals of the FBG sensors. The standard deviations of the FBG sensors 1, 2, and 3 are 1.10 pm, 1.29 pm, and 1.15 pm, respectively. The CV of wavelength migration error of the three fibers are 6.52%, 8.34%, and 4.78% respectively, which indicates that the repeatability of the fiber is stable. The FBG sensor decoder has wavelength repeatability of 1 pm. Its wavelength stability is usually 1–3 pm. Therefore, it can be concluded that the designed force sensor provides reliable repeatability, which is consistent with the inherent optical properties of the FBG decoder.

3.2. Force calibration

Based on the force calibration experiment, we calculate the calibration matrix K_i to describe the relationship between the transverse force F_x and F_y and the wavelengths $\Delta\lambda_1$, $\Delta\lambda_2$, and $\Delta\lambda_3$.

$$\begin{bmatrix} F_x \\ F_y \end{bmatrix} = \begin{bmatrix} K_{11} & K_{12} & K_{13} \\ K_{21} & K_{22} & K_{23} \end{bmatrix} \begin{bmatrix} \Delta\lambda_1 \\ \Delta\lambda_2 \\ \Delta\lambda_3 \end{bmatrix} \quad (15)$$

The X , Y , and Z components of the force F_P can be calculated as follows

$$F_x = \|F_w\| \sin(\alpha + \theta) \sin \beta \quad (16)$$

$$F_y = \|F_w\| \sin(\alpha + \theta) \cos \beta \quad (17)$$

$$F_z = \|F_w\| \cos(\alpha + \theta) \quad (18)$$

where F_w is the total force magnitude that equals the calibration weight.

The coefficient matrix K_i is calculated as

$$k_i = \begin{bmatrix} -0.0355 & 0.0424 & -0.0113 \\ -0.0201 & 0.0668 & -0.04 \end{bmatrix} \quad (19)$$

The wavelength resolution of the FBG decoder is 1 pm. Its transverse force resolution is about 0.067 mN, and the linear fitting results are depicted in Fig. 6. Fig. 6(a) and (b) illustrate the actual force and the calculation force. Obviously, the R^2 of the actual force F_x , F_y and the estimated force F_x , F_y are 0.98 and 0.99 respectively, and the fitting slope between the actual force and the calculated force is 1. It indicates that the actual force F_x , F_y are consistent with the calculated force F_x , F_y . The relationship between the residual error and the actual force is shown in Fig. 6(c) and (d). The root mean square (RMS) error is 0.0042 mN for F_x and 0.0038 mN for F_y . Fig. 6(e) and (f) show the probability distribution of F_x and F_y fitting residuals. The residual normal distribution functions of F_x and F_y are $N_x(0, 0.62)$ and $N_y(0, 0.68)$ respectively. The probability that all the residuals fall in the $[-0.1, 0.1]$ mN interval is higher than 95%, which indicates that the residuals are robust. A forced relationship exists between lateral force and axial force the resolution and residual error of axial force and lateral force are the same.

3.3. Temperature compensation

The purpose of this experiment is to verify the proposed temperature compensation algorithm for transverse force calculation. Considering that the manipulating temperature of zebrafish embryo cells is 28.5°C , this experiment verified the robustness of the designed sensor in the temperature range of $25-30^\circ\text{C}$. As shown in Fig. 7, this experiment adopts central air conditioning (KFR-72TW/(72550)NhCa-3. Gree Inc., China) to adjust the environment temperature, while a thermometer (TH101, Shenzhen DeFu Hardware Products Co., Ltd. China) is used to measure the indoor temperature. This experiment is divided into two steps. The first step is to adjust the ambient temperature to 25°C and then control the temperature change from 25 to 30°C . The second step is to lower the needle by the robot and apply a compression force in the range of 0–5 mN at intervals of approximately 1 mN.

As shown in Fig. 8, the wavelength of all FBG sensors is shifted with temperature change. The following analysis takes FBG1 as an example to illustrate the temperature compensation algorithm. When the environmental temperature changes from 25 to 30°C , the actual FBG1 can cause wavelength shift under empty load conditions. However, after using the temperature compensation algorithm in Eq. (3), it can be observed that the wavelength of the calculated FBG1 remains relatively constant. It demonstrates the effectiveness of the proposed temperature compensation algorithm.

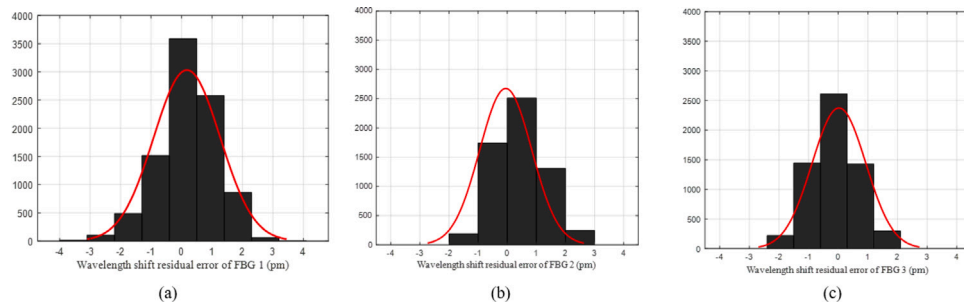


Fig. 5. The wavelength shift residual errors of the FBG sensor 1(a), 2(b), and 3(c). The probability distribution of wavelength shift residual errors shows the force sensor provides a reliable repeatability.

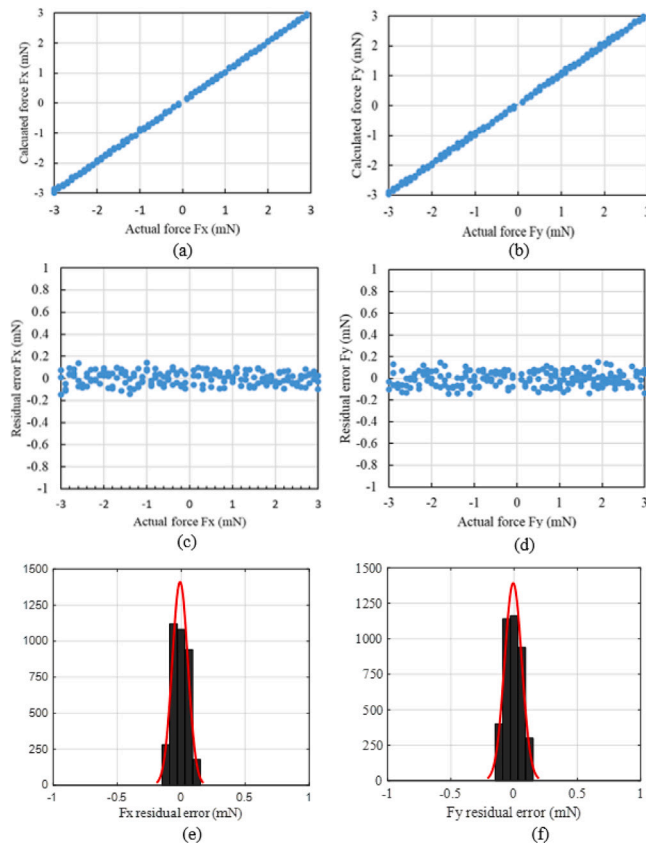


Fig. 6. The calculated transverse force along X -axis F_x versus the actual value using (a) linear fitting, (c) its residual error, and (e) the histogram of the residual error of F_x . (b) Calculated transverse force along Y -axis F_y versus the actual value using linear fitting, (d) its residual error, and (f) histogram of the residual error of F_y .

As shown in Fig. 9, it illustrates the robustness of the temperature compensation algorithm to axial forces when the temperature changes with the range from 25 to 30 °C. The designed sensor is able to keep the loading force values unchanged with the temperature variation. The actual force is close to the calculated force in this experiment. This experiment result shows that the proposed method can eliminate the influence of temperature on the wavelength shift of FBG. So it can be applied to characterize axial force robustly.

3.4. Cell deformation model

The puncture speed can affect the deformation and puncture force of the cell. To describe the relationship among cell deformation, puncture speed, and puncture force, a mechanical model is established as shown

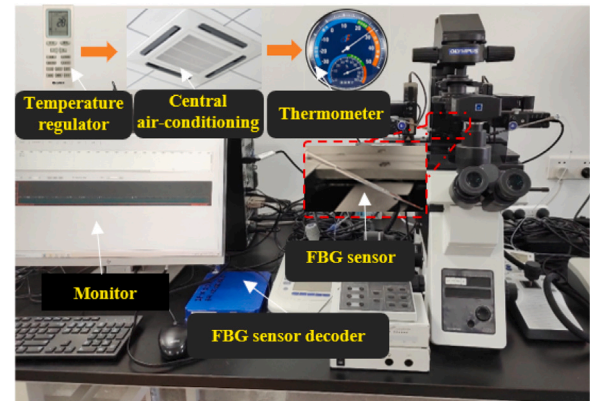


Fig. 7. Central air conditioning is used to control the indoor temperature, while a thermometer is used to measure the indoor temperature. The FBG sensor decoder records the wavelength shift of the FBG sensor.

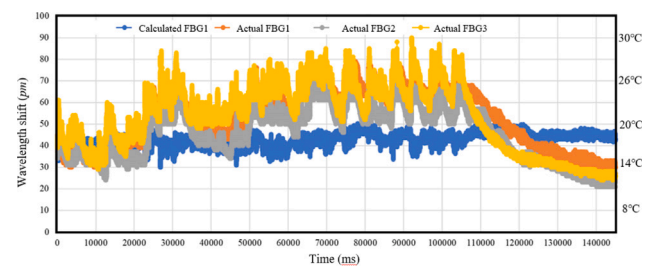


Fig. 8. Temperature compensation experiment. The central wavelength of FBG remains unchanged when the temperature changes with the range from 25 to 30 °C.

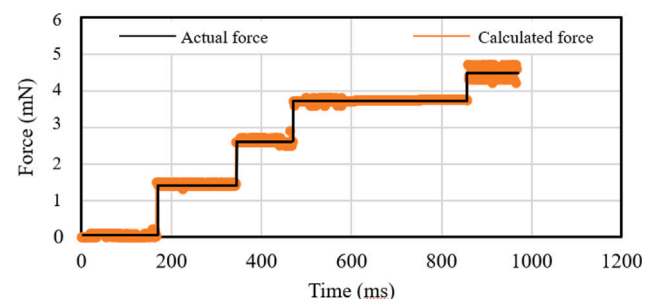


Fig. 9. Mechanical experiment under temperature change. It illustrates the robustness of the temperature compensation algorithm to axial forces when the temperature changes with the range from 25 to 30 °C.

in Fig. 10. A cell is a viscoelastic object, which is deformed and squeezed by the force. It is obvious that increasing the injection speed

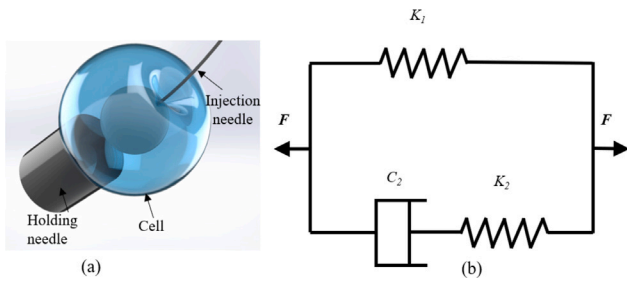


Fig. 10. (a) Schematic of cell injection, (b) Schematic of Maxwell-Wiechert model.

will reduce the cell deformation and increase the puncture force. The following assumptions are considered: (1) zebrafish embryonic cells are defined as a standard ball shape; (2) a uniform hydrostatic pressure is applied on the cell membrane; (3) the cell membrane thickness is uniform and the inner cytoplasm is defined as incompressible; (4) the oocyte volume is uniform and the elasticity of the membrane varies linearly. The Maxwell-Wiechert model is employed to demonstrate the reaction behavior of oocytes, which consists of a standard linear form Maxwell and a spring. K_1 , K_2 , and C_2 represent the elastic and viscoelastic behavior of the oocytes, respectively. The spring and dashpot equations are written as follows [31–33]

$$F = KX \quad (20)$$

$$F = CV = C \frac{dX}{dt} \quad (21)$$

where K and C represent the spring and damper constant, respectively. During cell puncture, the deformation of the cell is X , which represents the sum of the spring X_s and the deformation of the damper X_d . V is the puncture speed. The force is calculated as [32]

$$F(t) = KX_t e^{-\frac{Kt}{C}} \quad (22)$$

$$KX_s = C \left(\frac{dX_d}{dt} \right) \quad (23)$$

Eq. (22) can be written as

$$F(t) = CV e^{-\frac{Kt}{C}} \quad (24)$$

Finally, the resultant force for Maxwell-Wiechert model is expressed as [32–34]

$$F(t) = K_1 X_t + C_2 V e^{-\frac{K_2 t}{C_2}} \quad (25)$$

where K_1 , K_2 , C_2 denote spring and damper constants, respectively. Multiple groups of puncture velocity, cell deformation, and puncture force data are determined by the undetermined coefficient method. K_1 , K_2 , and C_2 are 0.75, -1.03 , and 6.83 , respectively. According to the Eq. (25), the model is

$$F(t) = 0.75X_t + 6.83V e^{\frac{1.03t}{6.83}} \quad (26)$$

This model describes the dynamic relationship between puncture force, cell deformation, and puncture speed, which can be used for cell deformation control.

3.5. Application of the microforce sensor in microinjection

In order to demonstrate the feasibility of the proposed sensor in microinjection, zebrafish embryonic cells are selected as the experimental object because they are important for the study of human diseases.

Cells are manipulated on a micromanipulation platform equipped with a microforce sensor. As shown in Fig. 11, the system consists of an inverted microscope (IX73P2F, Olympus Inc., Japan) equipped with an XYZ objective stage. The injection and holding needles are installed

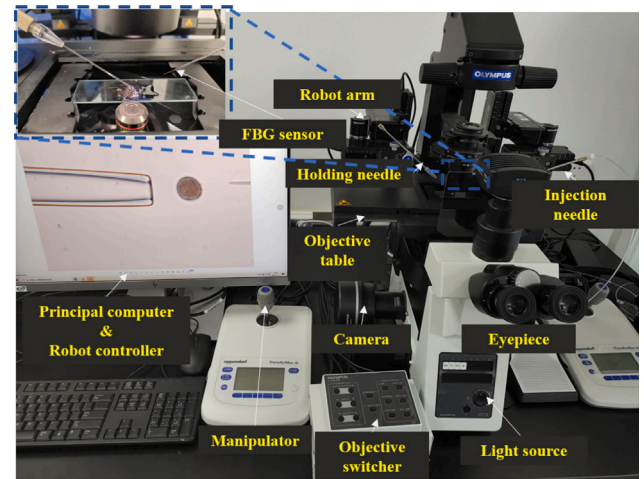


Fig. 11. Micromanipulation platform. The system consists of an inverted microscope equipped with an XYZ objective stage. The injection and holding needles are installed on a 12-degree-of-freedom (DOF) micromanipulation platform with two 3-DOF manipulators. A camera is attached to the microscope to capture images at 30 FPS.

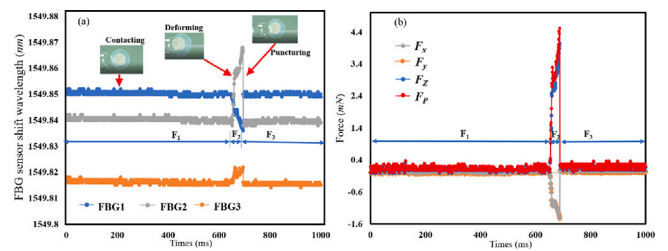


Fig. 12. Experiment results for cell puncture of zebrafish embryos. (a) The wavelength shift of the sensor during microinjection. (b) Puncture force during microinjection. Cell microinjection involves three processes: contacting, deforming, and puncturing. F_1 represents the force sensor signal before the cell deformation. F_2 represents the force sensor signal during the cell puncturing. F_3 represents the force sensor signal after the cell deformation. When the cell is pierced, the force sensor produces a distinct step signal.

on a 12-degree-of-freedom (DOF) micromanipulation platform with two 3-DOF manipulators (TransferMan 4r, Eppendorf Inc., Germany) with a kinematic resolution of $0.02 \mu\text{m}$. The motion speed range is $0\text{--}10,000 \mu\text{m/s}$. The holding needle is connected to the pneumatic pump used for cell aspiration. A complementary metal oxide semiconductor (CMOS) camera (DP74, Olympus Inc., Japan) is attached to the microscope to capture images at 30 FPS with a maximum resolution of 5760×3600 pixels. The microscope is operated in bright-field viewing mode, which provides the necessary optical magnification of $400\times$ and illumination levels for proper imaging of the injection area. In the experiment, the angle is 30° between the injection needle and the horizontal direction.

As shown in Fig. 12, F_1 represents the force sensor signal before the cell deformation, F_2 represents the force sensor signal during the cell puncturing, F_3 represents the force sensor signal after the cell deformation. It is significantly found that the force signal reached its maximum at the moment when the cell is punctured. F_2 is higher than F_1 and F_3 . At this moment, the total puncture force F_p of the cell is 4.277 mN , with F_x , F_y , and F_z being 1.488 mN , 1.535 mN , and 3.704 mN respectively. Based on the model illustrated in Eq. (26), the puncture speed of the robot is approximately $584 \mu\text{m/s}$ when the cell deformation is $300 \mu\text{m}$ and the puncture time is 100 ms . Although the force signal of the sensor has a certain noise, the noise signal is stable and about $1/15 - 1/30$ of the maximum puncture force. It indicates that the designed sensor can be used to characterize mechanical signals during cell puncture. The puncture experiment results of zebrafish

Table 2
Mechanical data of cell microinjection experiment.

Number	FBG1 (pm)	FBG2 (pm)	FBG3 (pm)	F_x (mN)	F_y (mN)	F_z (mN)	F_p (mN)
1	26	−12	5	−1.488	−1.535	3.704	4.277
2	30	7	5	−0.825	−0.350	1.550	1.790
3	−14	12	6	0.938	0.830	2.168	2.50
4	−12	22	5	1.302	1.500	3.440	3.971
5	−10	22	5	1.231	1.460	2.307	3.818
6	−8	19	5	1.033	1.219	2.767	3.195

embryos are recorded in Table 2, from which it can be seen that the experimental value of the 1st group is higher than other groups. The cells may be at late stages of growth and their Young's modulus is larger. Therefore, a greater force is required to penetrate the cell membrane.

For the designed sensor, The noise may be related to the tiny vibration of the injection needle or operating platform, or it may be the effect of ambient light on the sensor. Therefore, in future work, damping measures and sensor packaging technology will be adopted to reduce noise interference.

4. Discussion

This work proposes a novel microinjector with a force sensor that can be used for force monitoring during cell injection. The proposed microinjector has a three-dimensional force sensing capability, which benefited from the design of structural and mechanical estimation models. The sensor has four significant advantages. First, the proposed sensor exhibits a large measurement range (> 400 g) capability with a high resolution ($66.8 \mu\text{N}$). Second, the designed sensor is highly integrated with the glass needle. The sensor is affixed to the surface of the glass needle and can be installed directly onto an existing micro-manipulation platform without the need for additional clamps. Third, it can not only measure microforce but also inject foreign substances into cells. Most existing sensors in the previous work cannot provide such a function. Fourth, the designed sensor is low-cost and can be reused. The entire instrument costs no more than \$50 excluding the FBG sensor decoder, far less than other micro-force sensors. If the needle tip is broken, the sensor can be separated from the glass needle under the corrosion of sulfuric acid to realize the recycling of the fiber.

The accuracy of physical sensors is affected by temperature. In this work, a temperature compensation algorithm is presented to reduce the change of FBG center wavelength. Considering that the manipulating temperature of zebrafish embryo cells is 28.5°C , we perform an experiment with temperature ranging from 25 – 30°C , which adopted air conditioning as the heat source to simulate the ambient temperature change. Experiment results show that the proposed algorithm is effective. It is obvious that the previous work [5,25] did not take into account the effect of temperature on the physical components. To ensure the sensor calibration results, an electric mechanical calibration platform is established. It improves the calibration efficiency and the control accuracy of the needle pose compared with manual calibration.

As compared with the existing research on microinjection, the proposed method can inject exogenous substances into organisms or cells and record mechanical information to judge the cell puncture state. The designed sensor possesses a high load (> 400 g) and highly sensitive force-sensing ability (resolution: $66.8 \mu\text{N}$). Concerning the non-contacting type of micro force sensors for injection, e.g., visual force sensor and optical force sensor, these sensors highly relied on robust cell models or physical devices. For contact sensors, the comparison between this work and the existing sensors is summarized in Table 3. Although the sensors in literature [22,35,36] have high resolution, they are difficult to integrate with the hollow needle and sense the microforce during cell puncture. Due to these sensors cannot inject exogenous substances into cells, they are rarely applied

Table 3
Comparison of the existing force-sensing instruments for cell microinjection.

Sensor type	Resolution	Range	Inject function
Capacitive sensor [5]	$968 \mu\text{N}$	> 1 N	Yes
Capacitive sensor [22]	0.0678 nN	0 – $13.83 \mu\text{N}$	No
Piezoelectric sensor [35]	$4.3 \mu\text{N}$	0 – 13.83 mN	No
Piezoelectric sensor [28]	0.80 mN	0 – 1.23 mv/mN	Yes
Piezoresistive sensor [25]	0.65 mN	0 – 16.5 mN	Yes
Strain-gauge sensor [36]	$4.3 \mu\text{N}$ $56 \mu\text{N}$	$>2.5 \text{ mN}$ $>120 \text{ mN}$	No
This work	$66.8 \mu\text{N}$	$> 20 \text{ mN}$	Yes

in microinjections. For literature [5,25,28], these sensors are capable of injecting exogenous substances into cells. The proposed sensor in literature [5] has a large range, but the sensor resolution is lower than that proposed in literature [25].

5. Conclusion

In this work, a novel microforce sensor is designed to detect 3D forces for microinjection. The proposed sensor can detect transverse and axial forces, which can be used to judge the success of the cell puncture and adjust the robot motion parameters. It can also be applied reliably in temperature-changing environments. The force estimation model is calibrated by the mechanical calibrated platform, and the repeatability and reliability of the sensor are verified. The experiment results show that the designed force sensor can achieve a resolution of $66.8 \mu\text{N}$ for transverse force and axial force. The designed sensor has been applied for microinjection of the zebrafish embryo, which can reliably measure puncture force with a small temperature fluctuation. In addition, it can also be used to determine cell growth cycles. In future work, We will develop a self-protection system based on force sensors to enhance the interaction between the injector and cell.

CRediT authorship contribution statement

Xiangyu Guo: Conceptualization, Data curation, Formal analysis, Investigation, Methodology, Project administration, Software, Validation, Visualization, Writing – original draft, Writing – review & editing. **Antian Zhao:** Data curation, Writing – original draft. **Youchao Zhang:** Visualization, Investigation. **Huanyu Jiang:** Conceptualization, Methodology, Validation, Visualization. **Limin Zeng:** Software, Validation. **Alois Knoll:** Data curation, Resources, Supervision, Writing – review & editing. **Yibin Ying:** Methodology, Resources, Writing –

review & editing. **Mingchuan Zhou:** Conceptualization, Data curation, Formal analysis, Funding acquisition, Investigation, Methodology, Project administration, Resources, Supervision, Visualization, Writing – original draft, Writing – review & editing.

Declaration of competing interest

The authors declare that they have no known competing financial interests or personal relationships that could have appeared to influence the work reported in this paper.

Data availability

Data will be made available on request.

Acknowledgments

This study was supported by the ZJU100 Young Talent Program.

References

- [1] Changsheng Dai, Zhuoran Zhang, Yuchen Lu, Guanhao Shan, Xian Wang, Qili Zhao, Changhai Ru, Yu Sun, Robotic manipulation of deformable cells for orientation control, *IEEE Trans. Robot.* 36 (1) (2019) 271–283.
- [2] Xiangyu Guo, Youchao Zhang, Daoyuan Jin, Mingchuan Zhou, A review of single-cell pose adjustment and puncture, *Adv. Intell. Syst.* 4 (11) (2022) 2200096.
- [3] Changsheng Dai, Guanhao Shan, Xingjian Liu, Changhai Ru, Liming Xin, Yu Sun, Automated orientation control of motile deformable cells, *IEEE Trans. Autom. Sci. Eng.* (2022).
- [4] Yuzhang Wei, Qingsong Xu, A survey of force-assisted robotic cell microinjection technologies, *IEEE Trans. Autom. Sci. Eng.* 16 (2) (2018) 931–945.
- [5] Yuzhang Wei, Qian Zhou, Ziqiang Chi, Bing Ji, Bingpu Zhou, Qingsong Xu, Design and testing of a new microinjector with capacitive force sensor for biological microinjection, *IEEE Trans. Autom. Sci. Eng.* (2023).
- [6] Hang Yuan, Wenwen Yuan, Sixuan Duan, Keran Jiao, Quan Zhang, Eng Gee Lim, Min Chen, Chun Zhao, Peng Pan, Xinyu Liu, et al., Microfluidic-assisted caenorhabditis elegans sorting: Current status and future prospects, *Cyborg Bionic Syst.* 4 (2023) 0011.
- [7] Anand Pillarisetti, Maxim Pekarev, Ari D Brooks, Jaydev P Desai, Evaluating the effect of force feedback in cell injection, *IEEE Trans. Autom. Sci. Eng.* 4 (3) (2007) 322–331.
- [8] Zhijie Nan, Qingsong Xu, Yibo Zhang, Wei Ge, Force-sensing robotic microinjection system for automated multi-cell injection with consistent quality, *IEEE Access* 7 (2019) 55543–55553.
- [9] Xiangyu Guo, Youchao Zhang, Minxuan Cao, Qingyao Shu, Alois Knoll, Huanyu Jiang, Yibin Ying, Mingchuan Zhou, Mechanical force characterization of living cells based on needle deformation, *Adv. Mater. Interfaces* (2023) 2300293.
- [10] Sofie Permana, Edward Grant, Glenn M Walker, Jeffrey A Yoder, A review of automated microinjection systems for single cells in the embryogenesis stage, *IEEE/ASME Trans. Mechatronics* 21 (5) (2016) 2391–2404.
- [11] Yuzhang Wei, Qingsong Xu, An overview of micro-force sensing techniques, *Sensors Actuators A* 234 (2015) 359–374.
- [12] Weikang Hu, Yanmei Ma, Zhen Zhan, Danish Hussain, Chengzhi Hu, Robotic intracellular electrochemical sensing for adherent cells, *Cyborg Bionic Syst.* (2022).
- [13] Katsuhisa Sakaguchi, Kei Akimoto, Masanori Takaira, Ryu-ichiro Tanaka, Tatsuya Shimizu, Shinjiro Umez, Research article cell-based microfluidic device utilizing cell sheet technology, *Cyborg Bionic Syst.* (2022).
- [14] Guangwei Wang, Qingsong Xu, Design and precision position/force control of a piezo-driven microinjection system, *IEEE/ASME Trans. Mechatronics* 22 (4) (2017) 1744–1754.
- [15] Piyu Wang, Qingsong Xu, Design and testing of a flexure-based constant-force stage for biological cell micromanipulation, *IEEE Trans. Autom. Sci. Eng.* 15 (3) (2017) 1114–1126.
- [16] Youhua Tan, Dong Sun, Wenhao Huang, Shuk Han Cheng, Characterizing mechanical properties of biological cells by microinjection, *IEEE Trans. Nanobiosci.* 9 (3) (2010) 171–180.
- [17] Frank Juelicher, Karsten Kruse, Jacques Prost, J-F Joanny, Active behavior of the cytoskeleton, *Phys. Rep.* 449 (1–3) (2007) 3–28.
- [18] Hamid Ladjal, Jean-Luc Hanus, Antoine Ferreira, Micro-to-nano biomechanical modeling for assisted biological cell injection, *IEEE Trans. Biomed. Eng.* 60 (9) (2013) 2461–2471.
- [19] Xinyu Liu, Keekyoung Kim, Yong Zhang, Yu Sun, Nanonewton force sensing and control in microrobotic cell manipulation, *Int. J. Robot. Res.* 28 (8) (2009) 1065–1076.
- [20] XJ Zhang, S Zappe, RW Bernstein, O Sahin, C-C Chen, M Fish, MP Scott, O Solgaard, Micromachined silicon force sensor based on diffractive optical encoders for characterization of microinjection, *Sensors Actuators A* 114 (2–3) (2004) 197–203.
- [21] Jeongho Kim, HoYoon Lee, Sehyun Shin, Advances in the measurement of red blood cell deformability: A brief review, *J. Cellular Biotechnol.* 1 (1) (2015) 63–79.
- [22] Wendi Gao, Cunlang Liu, Xiangguang Han, Libo Zhao, Qijing Lin, Zhuangde Jiang, Dong Sun, A high resolution MEMS capacitive force sensor with bionic swallow comb arrays for ultralow multiphysics measurement, *IEEE Trans. Ind. Electron.* (2022).
- [23] Yu Sun, Bradley J. Nelson, David P. Potasek, Eniko Enikov, A bulk microfabricated multi-axis capacitive cellular force sensor using transverse comb drives, *J. Micromech. Microeng.* 12 (6) (2002) 832.
- [24] Felix Beyeler, Simon Muntwyler, Bradley J. Nelson, A six-axis MEMS force-torque sensor with micro-Newton and nano-Newtonmeter resolution, *J. Microelectromech. Syst.* 18 (2) (2009) 433–441.
- [25] Yuzhang Wei, Qingsong Xu, Design and testing of a new force-sensing cell microinjector based on small-stiffness compliant mechanism, *IEEE/ASME Trans. Mechatronics* 26 (2) (2020) 818–829.
- [26] Chang Liu, Rui Li, Young Li, Xiumei Lin, Kaichen Zhao, Qun Liu, Shuowen Wang, Xueqian Yang, Xuyang Shi, Yuting Ma, et al., Spatiotemporal mapping of gene expression landscapes and developmental trajectories during Zebrafish embryogenesis, *Dev. Cell* 57 (10) (2022) 1284–1298.
- [27] Yuzhang Wei, Qingsong Xu, Design and testing of a new force-sensing cell microinjector based on soft flexure mechanism, *IEEE Sens. J.* 19 (15) (2019) 6012–6019.
- [28] Yuzhang Wei, Qingsong Xu, Design of a PVDF-MFC force sensor for robot-assisted single cell microinjection, *IEEE Sens. J.* 17 (13) (2017) 3975–3982.
- [29] Andy Gijbels, Emmanuel B Vander Poorten, Peter Stalmans, Dominiek Reynaerts, Development and experimental validation of a force sensing needle for robotically assisted retinal vein cannulations, in: 2015 IEEE International Conference on Robotics and Automation, ICRA, IEEE, 2015, pp. 2270–2276.
- [30] Christian E Hamm, Rudolf Merkel, Olaf Springer, Piotr Jurkojc, Christian Maier, Kathrin Prechtel, Victor Smetacek, Architecture and material properties of diatom shells provide effective mechanical protection, *Nature* 421 (6925) (2003) 841–843.
- [31] Zhao Guilan, Influence of Viscous Dampers on Seismic Performance of Reinforced Concrete Frame Structures, (Master's thesis), Kunming University of Science and Technology, 2020.
- [32] Y. Galeano-Duque, P.K. Sharma, M. Mesa, Modulating the water behavior, microstructure, and viscoelasticity of plasma-derived hydrogels by adding silica nanoparticles with tailored chemical and colloidal properties, *Mater. Today Commun.* 34 (2023) 105243.
- [33] Amir M Hajiyavand, Mozafar Saadat, Alessandro Abena, Ferhat Sadak, Xiaochen Sun, Effect of injection speed on oocyte deformation in ICSI, *Micromachines* 10 (4) (2019) 226.
- [34] Fan Pengxuan, Chen Wujun, Zhao Bing, Hu Jianhui, Zhang Daxu, Fang Guangqiang, Peng Fujun, The mechanical constitutive model of shape memory polymer based on generalized Maxwell model, *J. Shanghai Jiao Tong Univ.* 52 (8) (2018) 969.
- [35] Yu Xie, Dong Sun, Ho Yan Gloria Tse, Chong Liu, Shuk Han Cheng, Force sensing and manipulation strategy in robot-assisted microinjection on ebrashif embryos, *IEEE/ASME Trans. Mechatronics* 16 (6) (2010) 1002–1010.
- [36] Juntian Qu, Qiyang Wu, Tyler Clancy, Qigao Fan, Xin Wang, Xinyu Liu, 3D-printed strain-gauge micro force sensors, *IEEE Sens. J.* 20 (13) (2020) 6971–6978.